

Article

Microstructure and Compressive Properties of Porous 2024Al-Al₃Zr Composites

Wenchang Zhang ^{1,2,3} , Kun Xu ^{1,2,3}, Wei Long ^{1,2,3,*}  and Xiaoping Zhou ^{1,2,3}¹ School of Materials and Chemical Engineering, Hubei University of Technology, Wuhan 430068, China² Key Laboratory of Green Materials for Light Industry of Hubei Provincial, Wuhan 430068, China³ Hubei Engineering Laboratory of Automotive Lightweight Materials and Processing, Wuhan 430068, China

* Correspondence: maillong1982@126.com

Abstract: Porous 2024Al-Al₃Zr composites were prepared by in situ and spatial scaffolding methods. As the Al₃Zr content increased from 5 wt.% to 30 wt.%, the binding of the powder in the pore wall increased and the defects in the composites decreased. The yield strength of the composites reached 28.11 MPa and the energy absorption capacity was 11.68 MJ/m³ at a Zr content of 20 wt.%, when the composites had the best compression and energy absorption performance. As the space scaffold content increased from 50% to 70%, the porosity of the composites then increased from 53.51% to 70.70%, but the apparent density gradually decreased from 1.46 g/cm³ to 0.92 g/cm³, leading to a gradual decrease in their compressive properties. In addition, by analysing the compression fracture morphology, the increase of Al₃Zr will reduce the stress concentration and hinder the crack growth, while too much Al₃Zr will lead to brittleness and reduce the performance.

Keywords: porous composite; space holder method; compression property; energy absorption



Citation: Zhang, W.; Xu, K.; Long, W.; Zhou, X. Microstructure and Compressive Properties of Porous 2024Al-Al₃Zr Composites. *Metals* **2022**, *12*, 2017. <https://doi.org/10.3390/met12122017>

Academic Editors: Noé Cheung and Matej Vesenjak

Received: 13 September 2022

Accepted: 22 November 2022

Published: 24 November 2022

Publisher's Note: MDPI stays neutral with regard to jurisdictional claims in published maps and institutional affiliations.



Copyright: © 2022 by the authors. Licensee MDPI, Basel, Switzerland. This article is an open access article distributed under the terms and conditions of the Creative Commons Attribution (CC BY) license (<https://creativecommons.org/licenses/by/4.0/>).

1. Introduction

Porous aluminium, as a widely used structural and functional material [1], has become a highly practical topic due to its low density, high specific surface area, high specific strength and light weight [2–5]. Its properties such as vibration damping, energy absorption, flame retardancy, sound absorption and heat dissipation have been widely studied [6–8]. The preparation methods of porous aluminium generally include the gas injection method [9], foaming method [10], mould casting method [11], deposition method [12] and space holder method [13]. However, the mechanical strength of pure aluminium and aluminium alloys prepared by the above methods is poor, which limits the application of porous materials. Therefore, to enhance the mechanical strength of the material, some researchers added the second phase to the porous aluminium to prepare composites. The in situ synthesis method is widely used because of its uniform distribution and tight bonding. Inoguchi [14] prepared in situ Al₃Ti/Al porous composites and the compression properties of porous materials improved by the combination of Al phase and Al₃Ti. Atturan [15] prepared an A357-TiB₂ porous composite and the mechanical strength is much higher than Al porous materials. In situ synthesis of reinforced particles in porous aluminium enhances the mechanical properties of the composites.

In recent years, in situ generation of Al₃X, such as Al₃Ni, Al₃Fe, Al₃Ti, and Al₃Zr, has been used in different composites due to their attractive properties. But among these, Al₃Zr has attracted much attention due to its low density (4.11 g/cm³), high melting point (1580 °C), high specific strength, high specific stiffness, excellent corrosion and wear resistance [16,17]. The lattice matching values of Al₃Zr (tetragonal structure) and α-Al (FCC structure) in the a and c/2 directions are 93% and 99.2%. The relatively high wettability contributes to a better dispersion of particles in the matrix, better grain refinement and better properties of composite [18]. Gupta and Danie [19] added K₂ZrF₆ salt into the aluminium melt to produce Al₃Zr particles, the Al₃Zr particles dispersed uniformly and refined

microstructure during the melting process, which significantly improved the strength of the material. Pourkhorshid [20] used mechanical alloying (MA) and a hot extrusion process to prepare Al/Al₃Zr composites, the Al₃Zr began with the nucleation of the metastable phase and then transformed into a stable tetragonal Al₃Zr structure. The tensile yield stress of obtained Al-10 wt.%Al₃Zr composites is 103 MPa, which is about twice that of pure aluminium (53 MPa). It can be seen that the in situ Al₃Zr has a good effect on the mechanical properties of composites. Nevertheless, the studies on the application of Al₃Zr to improve the mechanical properties of porous aluminium have not been fully investigated. In the present study, the effects of Zr and NaCl space holder content on the microstructure of porous Al₃Zr/2024Al composites with space holder and in situ synthesis method were investigated. Changes in the compressive and energy absorption characteristics were also studied.

2. Materials and Methods

Materials: Zr powder (China, MACKLIN, purity > 99%, d50: 48 µm), 2024Al alloy powder (China, Sinopharm Group Chemical Reagent Co., average particle size: 48 µm), the alloy composition is shown in Table 1 and NaCl space-holder powders (China, Shanghai Wokai Biotechnology Co., purity: A.R., average size: 100~500 µm) were used, the morphology of powders is shown in Figure 1a–c.

Table 1. Chemical composition of the 2024Al alloy (mass fraction, %).

Cu	Mg	Mn	Si	Fe	Zn	Others	Al
3.949	1.283	0.452	0.087	0.123	0.137	0.050	Bal.

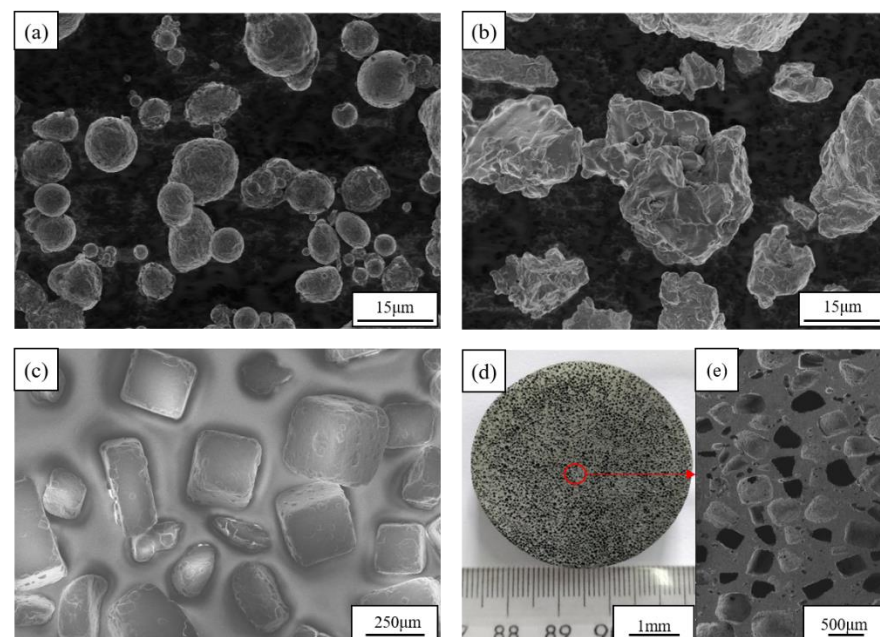


Figure 1. (a–c) SEM images of the raw powders: (a) 2024Al, (b) Zr, (c) NaCl. (d,e) the sample surface morphology of the sample.

Experimental procedures: First, 2024Al-Zr metal powder with Zr content of 5–30 wt.% was put into a planetary ball mill to mix the powder uniformly with a ball-to-ball ratio of 4:1 and a speed of 100 r/min for 3 h. In the second step, a 50–70 vol.% NaCl space holder was mixed uniformly with the above powder mixture with the same ball milling parameters as in the first step. The powder particle size was not changed before and after mixing. The final mixed powder was placed in the stainless-steel mould (inner diameter 40 mm, outer diameter 100 mm, height 100 mm), and the cold-pressed block with a height

of 10–12 mm was obtained by applying constant pressure (400 MPa). The block was heated to 650 °C at a heating rate of 5 °C/min in an argon atmosphere for 1 h [21]. The obtained sample was placed in water at 50 °C to remove NaCl. The sample surface morphology of the sample is shown in Figure 1d,e. The preparation and sintering process curves of the sample are shown in Figure 2.

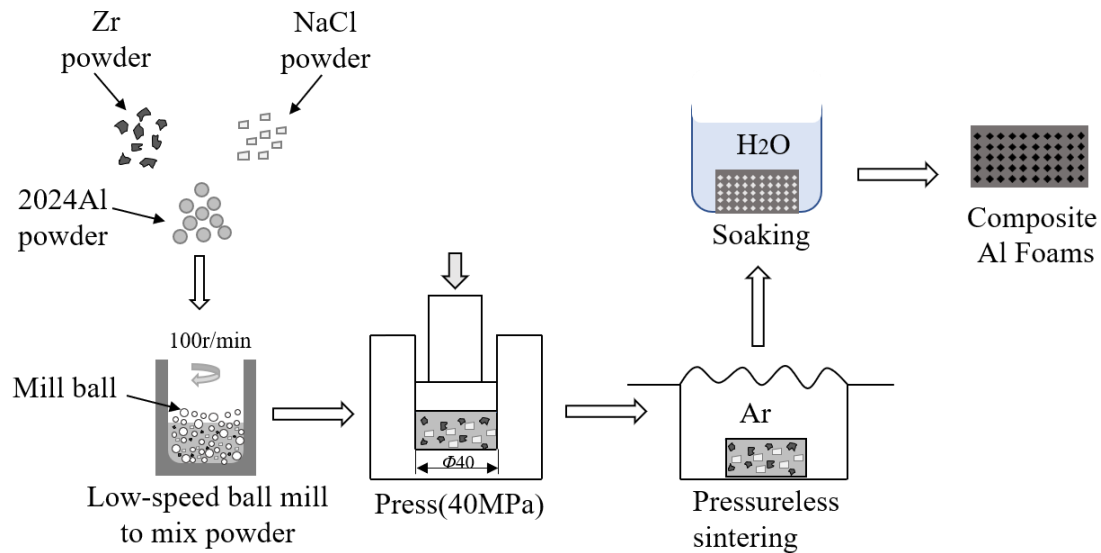


Figure 2. Schematic illustration showing the fabrication techniques for porous materials.

Characterisation of the porous composite: A rectangular compressed sample with a size of 10 × 10 × (10–12) mm was obtained through the wire electrical discharge machining. The porosity of the sample can be calculated by the following equation [22]:

$$P = 1 - \frac{m}{v\rho_s} \quad (1)$$

where m is the mass of the sample, v is the volume of the sample, and ρ_s is the theoretical density of the composite material, which can be calculated by the following equation [23]:

$$\rho_s = \frac{1}{\frac{m_{Al}}{\rho_{Al}} + \frac{m_{Zr}}{\rho_{Zr}}} \quad (2)$$

where m_{Al} , m_{Zr} are respectively mass fractions of 2024Al and Zr, the 2024Al is 2.78 g/cm³ and Zr is 6.49 g/cm³. In this study, to facilitate the description of the two types of pores studied and consequently the two sizes, we will use “intergranular pore” which corresponds to the pores between the particles (2024Al and Zr) in the matrix material and range from 1 to 10 μm. “Pores” correspond to the leached NaCl space holder which ranges from 100 to 500 μm. The intergranular porosity can be calculated in the following equation [24]:

$$P_m = P - P_n \quad (3)$$

where P_m is the intergranular porosity, P is the total porosity, P_n is the volume fraction of NaCl.

The compression test was carried out by the CMT-4204 material creep testing machine at room temperature. The previously mentioned rectangular compressed specimen of dimensions 10 × 10 × (10–12) mm was placed in the middle of the loading table at the strain rate of approximately $3.3 \times 10^{-3} \text{ s}^{-1}$. When the material was compressed to the

identified region, the compression stress–strain curve of the sample was obtained. The energy absorption capacity of the material is calculated by the following equation [25]:

$$\omega = \int_0^{e_0} \sigma \, de \quad (4)$$

where ω is the energy absorption capacity, e_0 is the densification strain and σ is the compressive stress. The compressive yield stress is defined as the first peak of the compressive stress–strain curve, and the plateau stress is set as the average stress in the range from 20% to 30% strain.

The micro-hardness of the pore wall of the sample was measured by a Vickers hardness tester with a load of 0.98 N (0.1 Kgf) along the vertical line. The hardness test was conducted at least ten test times, and the results were averaged. The phase composition of the composite was analysed through an Empyrean sharp shadow X-ray diffractometer at the scanning rate of $10^\circ/\text{min}$ with Cu-K α radiation; the obtained porous material was processed by wire cutting, mounting, polishing and cleaning, and the tissue was observed under an optical microscope. After it was determined that the surface of the material was free of scratches, the microstructure of the sample was observed by Zeiss Gemini 300 scanning electron microscope (SEM), and the phase composition was analysed by EDS.

3. Results and Discussion

3.1. Effect of Zr Content on Phase and Structure Morphology of Composites

Figure 3 presents the XRD pattern of the composites as an increase in the Zr content. As Zr content increases, the relative intensity of the Al peak decreases and the relative intensity of the Al_3Zr peak increases. The specimens were confirmed to be composed of $\alpha\text{-Al}(\text{fcc})$, $\text{Al}_3\text{Zr}(\text{D0}_{23})$ and $\text{Al}_2\text{Cu}(\text{C}_{16})$ phases, indicating that Zr reacted with Al to form Al_3Zr under the designed sintering process. The result was consistent with the Al-Zr binary phase diagram [26]. In the case where the mass fraction of Zr is less than 53%, Al and Zr will form a single-phase Al_3Zr intermetallic compound under equilibrium conditions. Moreover, there is no new phase formed involving the elements Na and Cl, reflecting that NaCl has no effect on the composition of the composite after sintering. It can be employed as an excellent space holder.

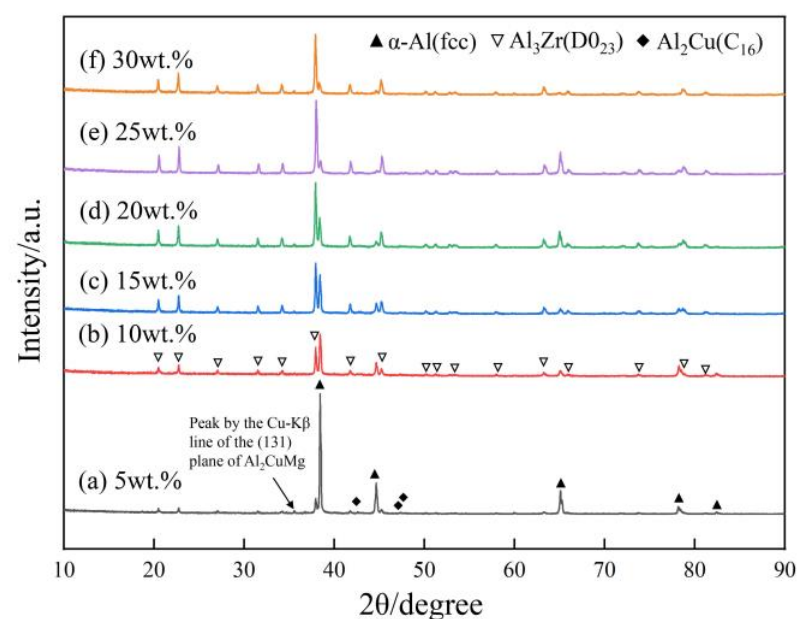


Figure 3. XRD patterns of the composites with different Zr contents.

Figure 4 shows the SEM image and results of the EDS quantitative analysis of composites with different Zr content. It can be concluded that the grey part is Al_3Zr and the morphology is mainly a fine block. In the case of Zr content 30 wt.%, the point scan result is Al_3Zr , which is consistent with the result of XRD, indicating that Zr and Al in this content will only form Al_3Zr and there is no other substance. An increase in Zr content also causes the appearance of Al_3Zr agglomerates with short rod morphology.

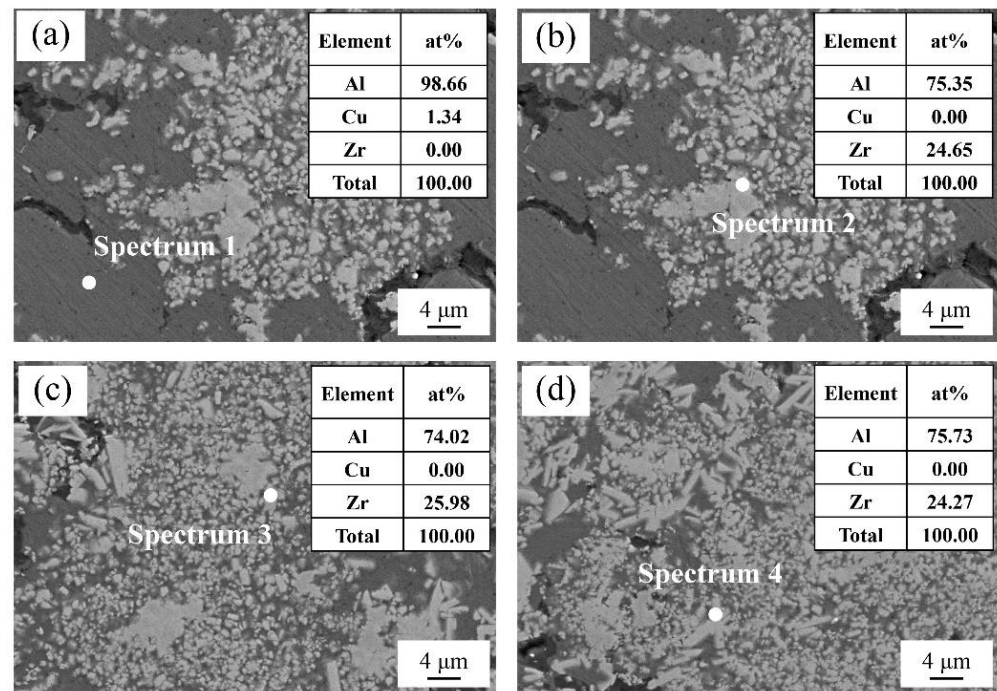


Figure 4. The points show the SEM images and results of EDS quantitative analysis of the $\text{Al}_3\text{Zr}/2024\text{Al}$ composites prepared with different Zr contents. (a,b) 10Zr; (c) 20Zr; (d) 30Zr.

Figure 5 is the SEM image of the pore wall of $\text{Al}_3\text{Zr}/2024\text{Al}$ porous composites with different Zr contents (space holder content is 60 vol.%). With the increase of Zr content, the number of Al_3Zr in the pore wall gradually increases, and the main components in the pore wall gradually change from 2024Al to Al_3Zr . As shown in Figure 5a,b, the Al_3Zr are mainly formed at the contact interface between Zr and 2024Al. In the region of the Al_3Zr phase, the microstructure was more uniform and regular compared with other regions, and there are fewer defects in the reaction area. However, obvious powder gaps and defects can be found between the mechanically bonded 2024Al powder particles, there is an obvious gap between the 2024Al powders, and there is much unevenness in the pore wall. When the Zr content continues to increase, the defect and gap in the material are declined and the distribution of Al_3Zr in the pore wall is more dispersed. In the case of Zr content 20 wt.%, the gap between 2024Al particles caused by mechanical bonding cannot be observed. It was supposed that the bonding mode of the material was metallurgical bonding. As the content of Zr further increases, a large number of 2024Al react with Zr. Almost the whole pore wall was occupied by Al_3Zr particles. It demonstrates that the material is mainly Al_3Zr . However, the amount of Al_3Zr possibly causes serious brittleness in the samples. The qualitative relationship between the content of Al_3Zr and the mechanical properties of the material will be investigated in the future.

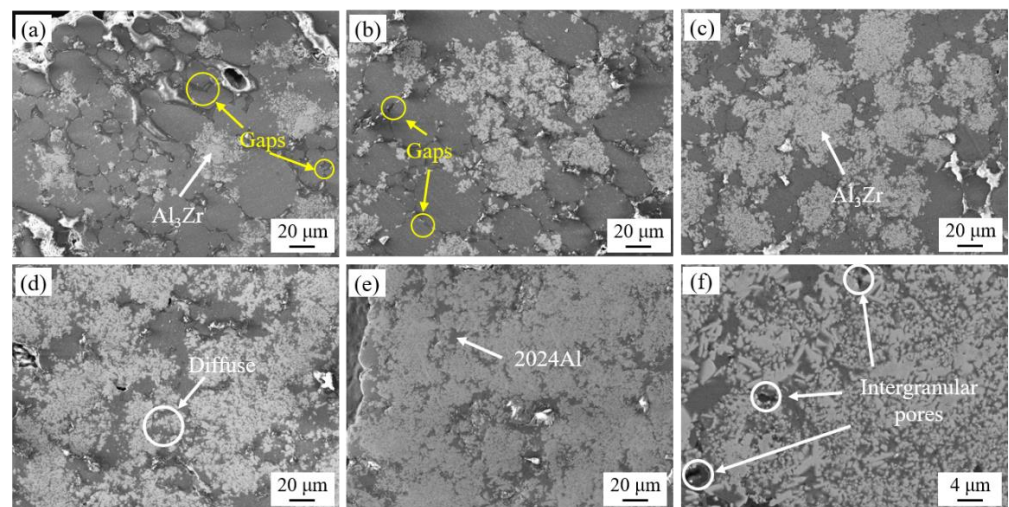


Figure 5. The SEM images of the composite pore wall were prepared with different Zr contents. (a) 5Zr; (b) 10Zr; (c) 15Zr; (d) 20Zr; (e) 25Zr; (f) 30Zr.

Figure 6 shows the SEM images of the pore walls of the porous composites. In the case of composition Zr5, there are obvious gaps (intergranular pores) between the crystals in the pore wall. This phenomenon occurred since the 2024Al in the sample melted at the sintering temperature of 650 °C and flowed out due to the low interfacial tension, which resulted in the precipitation of some aluminium alloy on the outside of the sintered sample. In contrast, the powder is tightly connected, and the gap is small, and the surrounding defects are greatly reduced at the composition Zr20. It illustrates that the Al_3Zr formation under the action of surface tension will prevent the outflow of molten 2024Al, even liquid phase sintering also can keep the shape of cold pressing, and the reaction heat between particles will accelerate the bonding between particles.

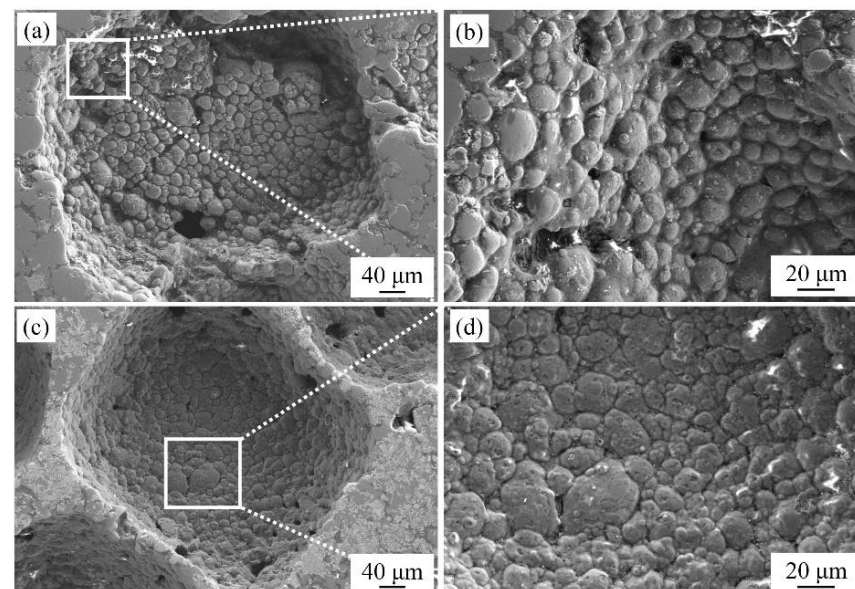


Figure 6. The SEM images of the pore walls of the porous composites with Zr content of (a,b) 5Zr and (c,d) 20Zr.

3.2. Effect of Zr Content on Mechanical Properties of Composites

Figure 7 shows the hardness of the pore wall of the composites with different Zr content. The hardness of the pore wall increases continuously with the increase of Zr content. Through the analysis of the hardness value, the highest hardness value (145.4 HV0.1) is

obtained in the case of Zr content 30 wt.%, which is 71.6% higher than that of 84.73HV0.1 in the case of Zr content 5 wt.%. Based on the above analysis, the low pore wall hardness of composites is attributed to the weak bonding of powder particles with low content of Al_3Zr . With the increase of Zr content, the main composition of the pore wall changes to Al_3Zr , leading to higher hardness.

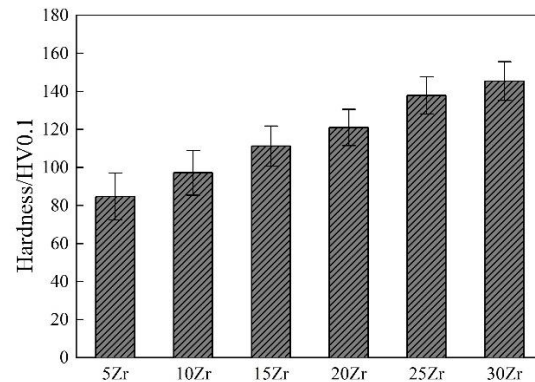


Figure 7. The hardness value of pore wall with different Zr content.

Figure 8 shows the compressive stress–strain and energy absorption capacity curves of the composites with different Zr content (space holder content is 60 vol.%). The curve in Figure 8a was divided into three regions: (1) Elastic region: the elastic deformation occurs, and the compression process is similar to dense materials, and the compression curve shows that the stress increases linearly with the increase of strain. The yield stress of the material is the value when the stress reaches the highest point for the first time. Moreover, the slope of the material with different Zr content in the elastic region is similar, indicating that the composition of the material has little effect on the elastic stage, and the main difference in the elastic region is the different yield stress of the material; (2) plateau region: most of the curves in this region is wavy or meandering. This phenomenon can be explained by the fact that the pore wall collapsed and deformed under the compressive load, and some pores ruptured rapidly with the increase of compressive strain, which eventually led to the stress weakening [27]. When the compression load is distributed to the uncompressed cavity, the support of the pore wall will make the stress increase again. So, the degree of curve bending is determined by the combined action of macroscopic and microstructural instability of porous materials [28,29]; (3) densified region: the pores in this area have been compacted, the material is in a dense state, and the compressive strain makes the stress rise rapidly.

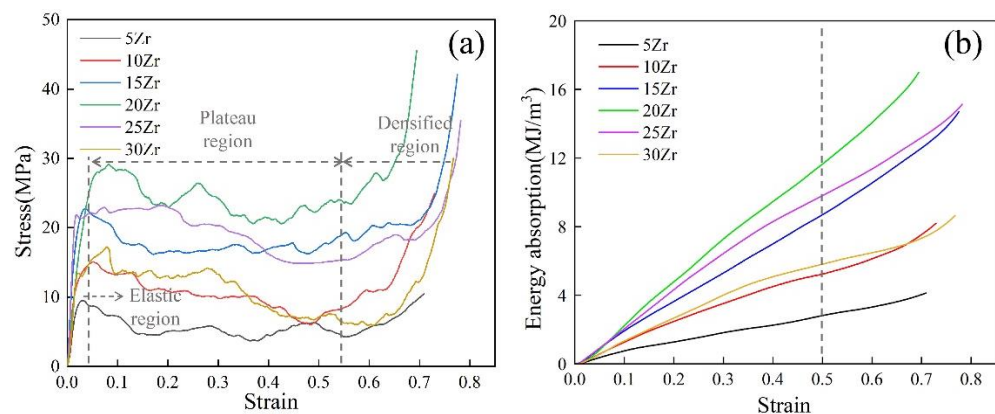


Figure 8. (a) Compressive stress–strain and (b) energy absorption capacity curves of composite materials with different Zr contents.

Compared with the upper limit of 50% strain, the curves in Figure 8b show that the energy absorption capacity of the material increases at first and then decreases with the increase of Zr content. In the case of Zr content 20 wt.%, the energy absorption capacity reaches the highest of 11.68 MJ/m^3 , which is 315.6% higher than that of 5Zr (2.81 MJ/m^3). This phenomenon can be explained by the fact that the energy absorption capacity is mainly related to the area under the stress–strain curve in the case of samples with similar porosity. Due to the good stiffness and elastic modulus of Al_3Zr , the performance of the material in the plateau stress region is improved as well as the energy absorption performance.

Figure 9 presents the yield stress and plateau stress of the composites with different Zr content. It can be seen that the numerical gap between yield stress and plateau stress decreases gradually. This phenomenon can be explained by the fact that the density of porous materials increased with the increase of Zr content, and the microstructure of the material gradually stabilised. Under the influence of these comprehensive factors, the plateau stress value gradually approached yield stress. The figure also shows that yield stress and plateau stress increase at first and then decrease with the increase of Zr content, and reached their highest point at a Zr content of 20 wt.%. The yield stress was 28.11 MPa, which was 198.1% higher than 5Zr (9.43 MPa), and the plateau stress was 24.87 MPa, 358.8% higher than 5Zr (5.42 MPa). Among them, the stress rise of the plateau is more than the yield stress, which is due to the low density and many defects in the case of Zr content 5 wt.%, the pores will collapse quickly after entering the plateau region, resulting in a rapid decrease in the platform stress.

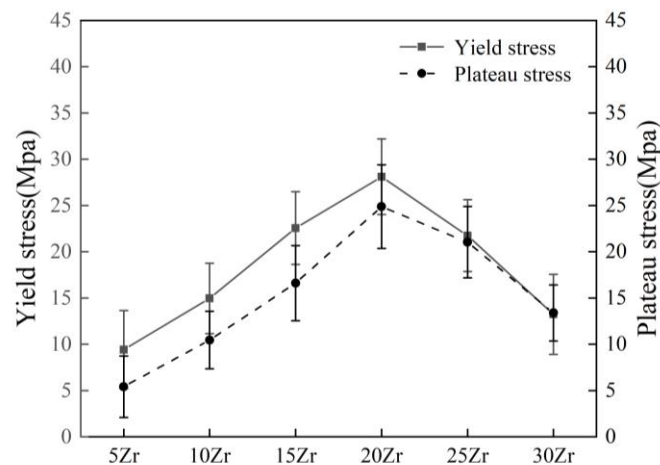


Figure 9. The yield stress and plateau stress of composites with different Zr contents.

In the case of Zr content 25 wt.% and 30 wt.%, there is mainly brittle phase Al_3Zr in the pore wall, cracks generated at defects will propagate easily, which could decline the material properties.

Figure 10 presents the SEM images of compression fracture of composites with different Zr contents. There are no obvious fracture characteristics in the area around the white box in Figure 10a, indicating that the white box area is one of the starting points for the fracture failure of the pore wall under the compression load. Moreover, some pore walls in the material are not in a strictly closed state, which causes the regional stress concentration, collapse and deformation in the compression process. At the fracture of Figure 10c, there are continuous dimples of different sizes, indicating that the fractured part is coherent. This may be due to the crack propagating in all directions because the thickness and structure of the pore wall are uniform, the fracture occurs in the whole area. However, it is difficult to directly observe the initial position of the fracture. Unlike the morphology of the sample in Figure 10c, there is a smooth area surrounded by cracks at the fracture of the pore wall in Figure 10e. Because the thickness distribution of the pore wall around this area is different and this irregular porous structure will cause stress concentration. The stress concentration in the thinner part of the pore wall will be greater than that in the

thicker pore wall, Zettl [30] also concluded that the initial defect is the preferred medial part of the pore wall and the damage begins in the thinner part of the pore wall.

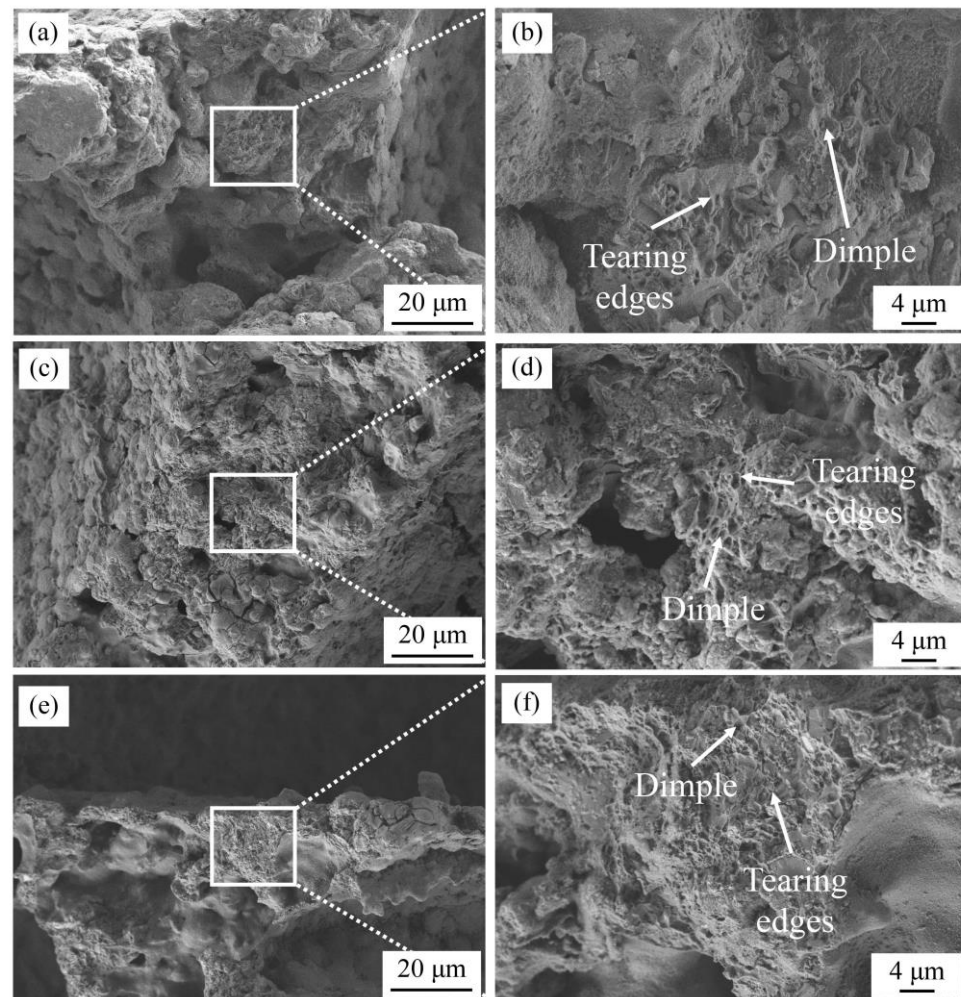


Figure 10. The SEM image of compression fracture of composites with different Zr content (a,b) 10Zr; (c,d) 20Zr; (e,f) 30Zr.

From the SEM of the pore walls, it can be seen that the fracture surfaces of 10Zr and 20Zr have a large number of dents and torn edges, indicating that the pore walls are ductile fractures. The dents of the fractures of 30Zr are larger and shallower than those of 20Zr, which indicates that brittle fractures occurred in the pore walls. Based on the explanation of the morphology and properties of porous materials with different Zr content, it can be considered that there are two fracture modes in the pore wall of $\text{Al}_3\text{Zr}/2024\text{Al}$ porous composites during compression. One is the fracture between ductile phase 2024Al, which is mainly displayed in Figure 10b. There are a large number of tear edges formed by the fracture between 2024Al. When the crack develops near the Al_3Zr particles, the fine Al_3Zr will hinder the crack extension and form dimples. As a result, the compression properties of the composites are enhanced. With the increase of the Al_3Zr number, the resistance of crack extension also increases, and the number of dimples in the fracture surface of the pore wall also increases. Another one is the brittle fracture of Al_3Zr , the interior of the material is mainly brittle phase Al_3Zr when too much Al_3Zr is formed. Due to the lack of ductile phase as support, the crack will develop rapidly after compression fracture, which leads to the fracture of some agglomerated Al_3Zr particles earlier than the ductile phase and makes the dimples on the fracture surface larger and shallower. Finally, this brittle structure causes the decline of material properties.

According to the previous explanation of pore wall morphology, the reaction of Zr and 2024Al from 5Zr to 20Zr forms finely dispersed Al_3Zr particles that hinder crack growth by reducing the stress concentration. The reaction also improved the density and reduced the number of defects on the pore wall. Under the combined effect of these factors, the composite performance is significantly improved. However, when the Zr content continues to increase, the composite is mainly brittle phase Al_3Zr , the crack will quickly spread to the surrounding parts under a compression load, thereby degrading the properties of the sample. Therefore, Al_3Zr should be composited with toughness to compensate for its brittleness, to obtain porous composites with excellent compressive and energy-absorbing properties.

3.3. Effect of Space Holder Content on Morphology and Properties of Composites

Figure 11 shows the morphology of the samples with different space holder contents (20 wt.% Zr content). Figure 11a,c,e show the macroscopic morphology of the specimens with space holder contents of 50 vol.%, 60 vol.% and 70 vol.%, where the morphology can remain intact after the removal of the space holder by impregnation. However, in the case of space holder content greater than 70 vol.%, some areas of the sintered specimens were difficult to maintain integrity due to the clumping of the space holder during cold pressing and collapse or detachment during impregnation, so porous specimens with space holder content greater than 70 vol.% were not explored in this paper. Figure 11b,d,f shows the enlarged shapes of specimens with 50 vol.%, 60 vol.% and 70 vol.% space holders. After removing the NaCl space holder by immersion, the macroscopic pores basically maintain the original shape of the NaCl particles, and with the increase of the space holder, the pores are more frequently connected, and the pore wall thickness gradually decreases.

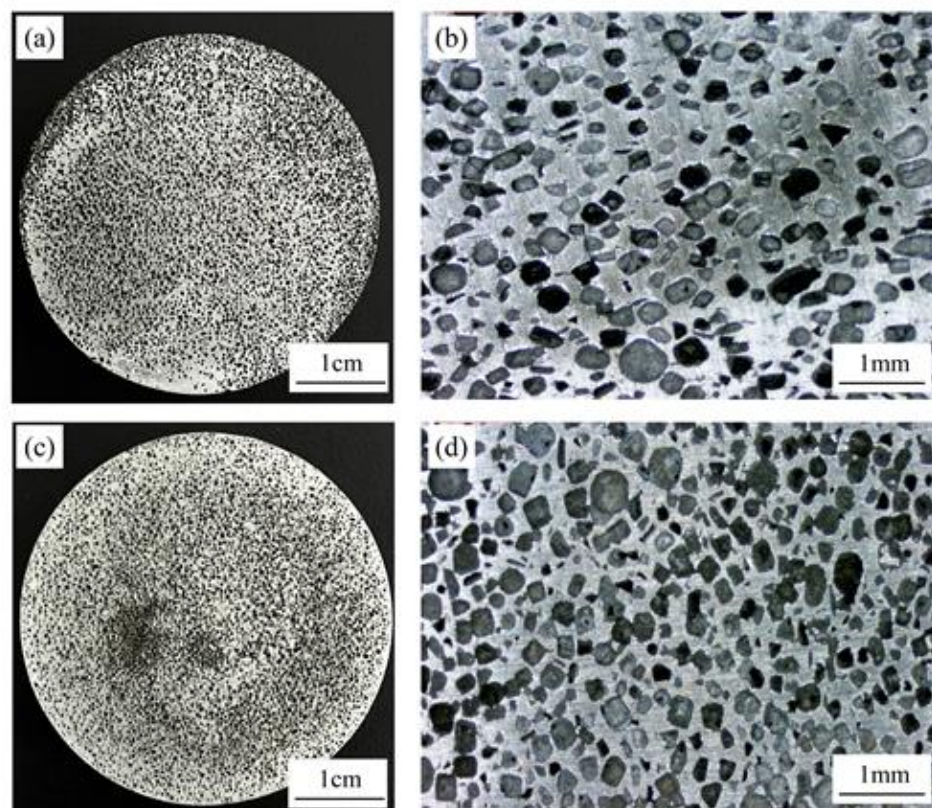


Figure 11. Cont.

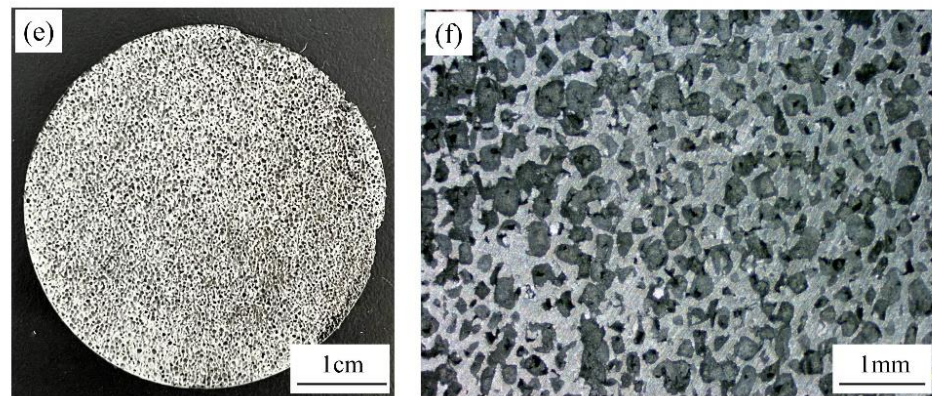


Figure 11. Macroscopic morphologies of porous materials with different contents of NaCl space holder (a,b) 50 vol.%; (c,d) 60 vol.%; (e,f) 70 vol.%.

This section introduces the relative density data according to the literature [30] investigation to better study the effects of different space holder contents on material properties [30]. The relative density is the ratio of the apparent density of the porous material to the theoretical density when the material is densified. Table 2 shows the mass, volume, apparent density and theoretical density of the 20Zr samples with different space holder percentages.

Table 2. The mass, volume, apparent density and theoretical density of the 20Zr samples with different space holder percentages.

Space Holder Percent/%	Mass/g	Volume/cm ³	Apparent Density/(g/cm ³)	Theoretical Density/(g/cm ³)
50	1.61	1 × 1 × 1.1	1.46	3.14
55	1.32	1 × 1 × 1.0	1.32	3.14
60	1.31	1 × 1 × 1.1	1.19	3.14
65	1.28	1 × 1 × 1.2	1.07	3.14
70	1.10	1 × 1 × 1.2	0.92	3.14

Relative density is also another manifestation of the density of the material, which can be calculated by the following equation [31]:

$$R = \frac{\rho_p}{\rho_s} \quad (5)$$

where R is the relative density, ρ_p is the apparent density of porous materials and ρ_s is the theoretical density of materials when they are dense. Table 3 shows the porosity, intergranular porosity and relative density of the composites with different space holder contents. It illuminates that with the increase of space holder content, the number of intergranular pores decreases gradually, and the porosity of the material is closer to the volume fraction of the space holder. This is due to the reduction of metal powder, the powder gap caused by cold pressing and the Kirkendall voids formed by the in situ reaction is also reduced [32], and the pores of porous materials are mainly formed by space holders.

Figure 12 shows the compressive stress–strain and energy absorption capacity curves with different relative densities (20Zr). It can be found that with the increase of porosity, the elastic strain limit and the slope of the curve decrease, and the yield stress of materials also decreases gradually. The plateau region in the curves is longer and flatter with the decreases in relative density. It is because porous materials with lower relative density (or higher porosity) have more pore structures. When the pore wall collapses and deforms under a compression load, there is enough space inside to bear the deformation of the pore wall. From the energy absorption capacity curve, it can be concluded that the energy

absorption performance of the porous material has a positive correlation with the relative density, because when the relative density is higher, there are more matrix materials in the porous material, and the compressive performance of the material will be better. Therefore, with the decrease in relative density, the energy absorption capacity also decreases.

Table 3. The porosity, intergranular porosity and relative density of the composites sintering at different space holder percentages.

Space Holder Percent/%	Porosity/%	Intergranular Porosity Porosity/%	Relative Density
50	53.51	3.51	0.47
55	57.96	2.96	0.42
60	62.10	2.10	0.38
65	65.92	0.92	0.34
70	70.70	0.70	0.29

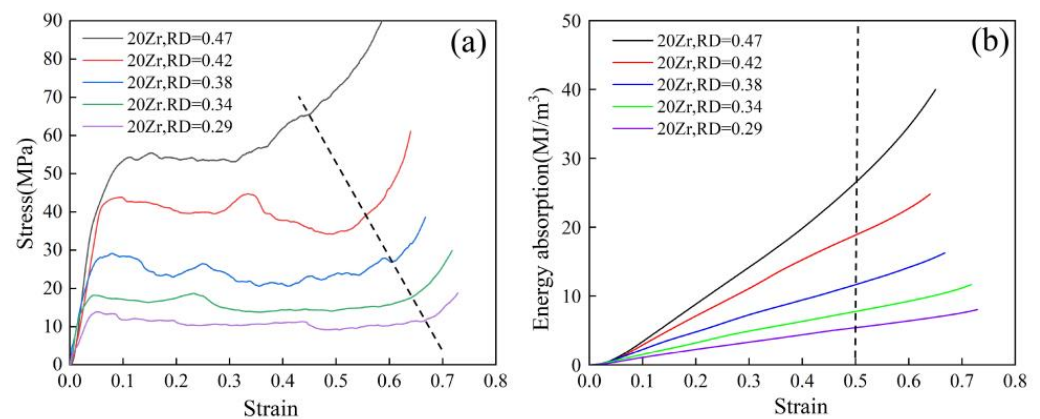


Figure 12. (a) Compressive stress–strain and (b) energy absorption capacity curves of composite materials with different relative densities.

Figure 13 shows the yield stress and plateau stress of the composites with different relative densities. It can be seen that the performance range of porous materials increases with the increase of relative density. This rule is mainly because with the increase of porosity, the space of the pore wall in the same area is smaller, and the thickness of the pore wall is thinner, the supporting capacity to the load decreases greatly, so the performance of the porous material decreases gradually. However, the decline in performance brings a larger specific surface area and lower density.

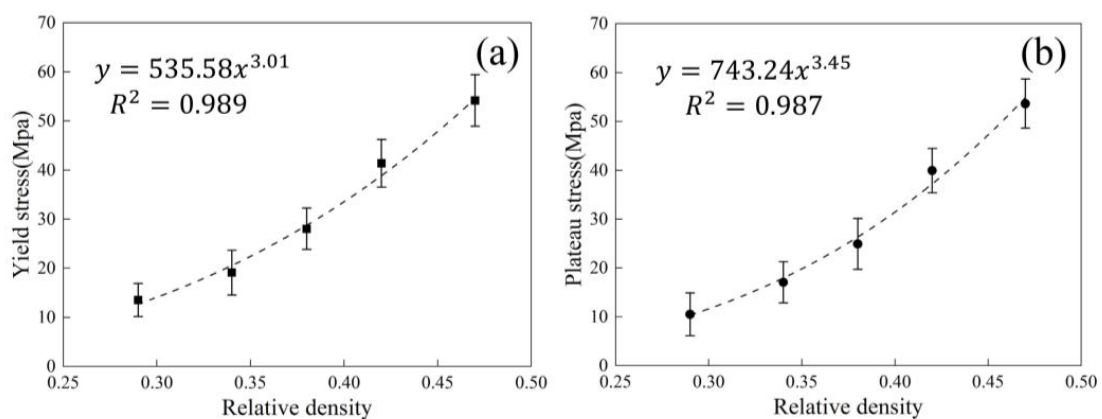


Figure 13. (a) Yield stress and (b) plateau stress of composites at different relative densities.

By comparing the prepared Al₃Zr/2024Al porous composites with other references, the properties of the materials are significantly improved, and the corresponding results are shown in Table 4. It is worth noting that the properties of porous composites prepared by in situ synthesis are better than those of pure aluminium, indicating that in situ synthesis has a unique advantage in solving the poor properties of porous aluminium.

Table 4. Compression properties of different porous materials.

Composition	Porosity/%	Yield Stress/MPa	Plateau Stress/MPa	Reference
Al ₃ Zr/2024Al	53.51	54.15	53.63	Present study
	62.10	28.02	24.94	
	70.70	13.52	10.51	
Al ₃ Ti/Al	~70	13	10	[32]
CNT/Al	~60	22.24	33	[22]
SiC/Al	~40	58	-	[33]
Al ₂ O ₃ /Al	~60	15	10	[34]
Al	~50	17.0	-	[35]
	~60	11.2	-	
	~70	4.6	-	

To better describe the effect of the relative density of porous materials on the compression properties of porous materials, Gibson and Ashby [6] assume that the pore wall is a dense material, and the compression of porous materials is mainly accomplished by the buckling and compression of the pore wall, and its strength is mainly determined by its relative density. A prediction model is proposed for this assumption, which can be calculated by the following equation [6]:

$$\sigma = 0.3 \left(\Phi \frac{\rho_f}{\rho_d} \right)^{\frac{3}{2}} + 0.4(1 - \Phi) \frac{\rho_f}{\rho_d} \quad (6)$$

where σ is the compressive strength of the porous material, ρ_f is the actual density of the porous material and ρ_d is the theoretical density when the material is fully dense, Φ is the volume percentage of the pore wall of the material. Because the porous material prepared by the space holder method is a three-dimensional reticular structure, after the space holder is removed, the whole material is composed of a pore wall, so the $\Phi = 1$. Therefore, D.P. Mondal [36] has made some modifications to this model, and the result is the following equation [36]:

$$\sigma = C \left(\frac{\rho_f}{\rho_d} \right)^n \quad (7)$$

where C and n are constant, determined by the properties of the porous material. This equation shows that the relationship between compression properties and the relative density of porous materials is exponential. Applying this equation to this experiment, the relationship between yield stress, plateau stress and relative density is as follows:

$$\sigma_y = 535.58 \left(\frac{\rho_f}{\rho_d} \right)^{3.01} \quad (8)$$

$$\sigma_p = 743.24 \left(\frac{\rho_f}{\rho_d} \right)^{3.45} \quad (9)$$

where σ_y is the yield stress, σ_p is the plateau stress. However, the pore wall of the actual porous material is difficult to be completely dense, and there will inevitably be some defects in the interior, and its pore structure, such as wall thickness and pore size cannot be the

same, and the distribution of pores is also difficult to achieve uniform distribution. But these equations can be used to predict the compressibility of porous materials, which will become a part of the production process route design in actual production.

4. Conclusions

The effects of differences on the microstructure and properties of Al₃Zr/2024Al porous composites were studied.

- (1) As the Zr content increases from 5 wt.% to 30 wt.%, the Al₃Zr content gradually increases, the pore walls become denser and the number of defects decreases. The hardness of the material also increases with the increase of Al₃Zr content from 84.73 HV0.1 to 145.4 HV0.1. The pressure properties and energy absorption properties first increase and then decrease, and the best overall performance is achieved with a compressive strength of 28.11 MPa and an energy absorption capacity of 11.68 MJ/m³ at a Zr content of 20 wt.%.
- (2) The compressive fractures of materials with different Zr contents show that Al₃Zr can improve the compressive properties of the material by hindering the propagation of cracks in the pore wall, but when the Al₃Zr content is too much, the pore wall will undergo brittle fracture and the performance will decrease.
- (3) As the space frame content increases from 50% to 70%, the relative density of the material gradually decreases from 0.47 to 0.29, and the yield strength and platform stress subsequently show a power function trend from 54.15 MPa and 53.63 MPa to 13.52 MPa and 10.51 MPa, respectively. Thus, the compressive properties and energy absorption capacity of the material gradually decrease.

Therefore, porous composites with excellent compression and energy absorption properties can be obtained by combining the brittle phase and ductile phase of Al₃Zr.

Author Contributions: Conceptualization and formal analysis, X.Z.; methodology and investigation, K.X.; data curation and writing—original draft preparation, W.Z.; writing—review and editing and supervision, W.L. All authors have read and agreed to the published version of the manuscript.

Funding: This research received no external funding.

Data Availability Statement: Data available on request due to restrictions eg privacy or ethics. The data presented in this study are available on request from the corresponding author. The data are not publicly available.

Conflicts of Interest: The authors declare that we have no known competing financial interests or personal relationships that might influence the work reported herein, and that the authors unanimously agreed to submit the manuscript to your journal.

References

1. Colombo, P.; Degischer, H.P. Highly Porous Metals and Ceramics. *Mater. Sci. Technol.* **2013**, *26*, 1145–1158. [[CrossRef](#)]
2. Esmaealzadeh, S.; Simchi, A.; Lehmhus, D. Effect of Ceramic Particle Addition on the Foaming Behavior, Cell Structure and Mechanical Properties of P/M AlSi7 Foam. *Mater. Sci. Eng. A* **2006**, *424*, 290–299. [[CrossRef](#)]
3. Shishkin, A.; Mironov, V.; Zemchenkov, V.; Antonov, M.; Hussainova, I. Hybrid Syntactic Foams of Metal—Fly Ash Cenosphere—Clay. *Key Eng. Mater.* **2016**, *674*, 35–40. [[CrossRef](#)]
4. Shishkin, A.; Drozdova, M.; Kozlov, V.; Hussainova, I.; Lehmhus, D. Vibration-Assisted Sputter Coating of Cenospheres: A New Approach for Realizing Cu-Based Metal Matrix Syntactic Foams. *Metals* **2017**, *7*, 16. [[CrossRef](#)]
5. Shishkin, A.; Hussainova, I.; Kozlov, V.; Lisnanskis, M.; Leroy, P.; Lehmhus, D. Metal-Coated Cenospheres Obtained Via Magnetron Sputter Coating: A New Precursor for Syntactic Foams. *J. Miner. Met. Mater. Soc.* **2018**, *70*, 1319–1325. [[CrossRef](#)]
6. Gibson, L.J.; Ashby, M.F. *Cellular Solids: Structure and Properties*; Cambridge University Press: Cambridge, UK, 1997.
7. Parveez, B.; Jamal, N.A.; Maleque, A.; Yusof, F.; Jamadon, N.H.; Adzila, S. Review on Advances in Porous Al Composites and the Possible Way Forward. *J. Mater. Res. Technol.* **2021**, *14*, 2017–2038. [[CrossRef](#)]
8. Ning, J.; Li, Y.; Zhao, G. Simple Multi-Sections Unit-Cell Model for Sound Absorption Characteristics of Lotus-Type Porous Metals. *Phys. Fluids* **2019**, *31*, 077102.
9. Wang, N.; Maire, E.; Chen, X.; Adrien, J.; Li, Y.; Amani, Y.; Hu, L.; Cheng, Y. Compressive Performance and Deformation Mechanism of the Dynamic Gas Injection Aluminum Foams. *Mater. Charact.* **2019**, *147*, 11–20. [[CrossRef](#)]

10. Yang, D.-H.; Chen, J.-Q.; Wang, L.; Jiang, J.-H.; Ma, A.-B. Fabrication of Al Foam without Thickening Process through Melt-Foaming Method. *J. Iron. Steel Res. Int.* **2018**, *25*, 90–98. [[CrossRef](#)]
11. Kubelka, P.; Körte, F.; Heimann, J.; Xiong, X.; Jost, N. Investigation of a Template-Based Process Chain for Investment Casting of Open-Cell Metal Foams. *Adv. Eng. Mater.* **2022**, *24*, 2100608. [[CrossRef](#)]
12. Shi, X.; Xu, G.; Liang, S.; Li, C.; Guo, S.; Xie, X.; Ma, X.; Zhou, J. Homogeneous Deposition of Zinc on Three-Dimensional Porous Copper Foam as a Superior Zinc Metal Anode. *ACS Sustain. Chem. Eng.* **2019**, *7*, 17737–17746. [[CrossRef](#)]
13. Jain, H.; Mondal, D.; Gupta, G.; Kumar, R.; Singh, S. Synthesis and Characterization of 316L Stainless Steel Foam Made through Two Different Removal Process of Space Holder Method. *Manuf. Lett.* **2020**, *26*, 33–36. [[CrossRef](#)]
14. Inoguchi, N.; Kobashi, M.; Kanetake, N. Synthesis of Porous Al₃Ti/Al Composite and Effect of Precursor Processing Condition on Cell Morphology. *Mater. Trans.* **2009**, *50*, 2609–2614. [[CrossRef](#)]
15. Atturan, U.A.; Nandam, S.H.; Murty, B.; Sankaran, S. Deformation Behaviour of in-Situ TiB₂ Reinforced A357 Aluminium Alloy Composite Foams under Compressive and Impact Loading. *Mater. Sci. Eng. A* **2017**, *684*, 178–185. [[CrossRef](#)]
16. Morere, B.; Shahani, R.; Maurice, C.; Driver, J. The Influence of Al₃Zr Dispersoids on the Recrystallization of Hot-Deformed Aa 7010 Alloys. *Metall. Mater. Trans. A* **2001**, *32*, 625–632. [[CrossRef](#)]
17. Gautam, G.; Mohan, A. Effect of ZrB₂ Particles on the Microstructure and Mechanical Properties of Hybrid (ZrB₂+ Al₃Zr)/Aa5052 In Situ Composites. *J. Alloys Compd.* **2015**, *649*, 174–183. [[CrossRef](#)]
18. Varin, R. Intermetallic-Reinforced Light-Metal Matrix in-Situ Composites. *Met. Mater. Trans. A* **2002**, *33*, 193–201. [[CrossRef](#)]
19. Gupta, R.; Daniel, B. Strengthening Mechanisms in Al₃Zr-Reinforced Aluminum Composite Prepared by Ultrasonic Assisted Casting. *J. Mater. Eng. Perform.* **2021**, *30*, 2504–2513. [[CrossRef](#)]
20. Pourkhorshid, E.; Enayati, M.H.; Sabooni, S.; Karimzadeh, F.; Paydar, M.H. Bulk Al–Al₃Zr Composite Prepared by Mechanical Alloying and Hot Extrusion for High-Temperature Applications. *Int. J. Miner. Metall. Mater.* **2017**, *24*, 937–942. [[CrossRef](#)]
21. Xun, K.; Dai, W.; Liu, N.; Zhang, W.; Long, W.; Zhou, X. Effect of Sintering Temperature on Microstructure and Compressive Properties of Al₃Zr/2024Al Porous Composites. *Trans. Mater. HT.* **2022**, *43*, 20–27.
22. Yang, K.; Yang, X.; Liu, E.; Shi, C.; Ma, L.; He, C.; Li, Q.; Li, J.; Zhao, N. Elevated Temperature Compressive Properties and Energy Absorption Response of in-Situ Grown Cnt-Reinforced Al Composite Foams. *Mater. Sci. Eng. A* **2017**, *690*, 294–302. [[CrossRef](#)]
23. Moreira, R.C.S.; Kovalenko, O.; Souza, D.; Reis, R.P. Metal Matrix Composite Material Reinforced with Metal Wire and Produced with Gas Metal Arc Welding. *J. Compos. Mater.* **2019**, *53*, 4411–4426. [[CrossRef](#)]
24. Shu, Y.; Suzuki, A.; Takata, N.; Kobashi, M. Fabrication of Porous NiAl Intermetallic Compounds with a Hierarchical Open-Cell Structure by Combustion Synthesis Reaction and Space Holder Method. *J. Mater. Process. Technol.* **2019**, *264*, 182–189. [[CrossRef](#)]
25. Bafti, H.; Habibolahzadeh, A. Production of Aluminum Foam by Spherical Carbamide Space Holder Technique-Processing Parameters. *Mater. Des.* **2010**, *31*, 4122–4129. [[CrossRef](#)]
26. Tamim, R.; Mahdouk, K. Thermodynamic Reassessment of the Al–Zr Binary System. *J. Therm. Anal. Calorim.* **2018**, *131*, 1187–1200. [[CrossRef](#)]
27. Zhao, A.; Qiu, S.; Hu, Y. Effect of Parametric Variations on the Local Compression Deformation of Aluminum Foam Sandwich Panels. *Mater. Trans.* **2017**, *58*, 880–885. [[CrossRef](#)]
28. Luo, Y.; Yu, S.; Li, W.; Liu, J.; Wei, M. Compressive Behavior of SiCp/AlSi9Mg Composite Foams. *J. Alloys Compd.* **2008**, *460*, 294–298. [[CrossRef](#)]
29. Raj, R.E.; Daniel, B. Aluminum Melt Foam Processing for Light-Weight Structures. *Mater. Manuf. Process.* **2007**, *22*, 525–530. [[CrossRef](#)]
30. Zettl, B.; Mayer, H.; Stanzl-Tscheegg, S.; Degischer, H. Fatigue Properties of Aluminium Foams at High Numbers of Cycles. *Mater. Sci. Eng. A* **2000**, *292*, 1–7. [[CrossRef](#)]
31. Jain, H.; Gupta, G.; Kumar, R.; Mondal, D.P. Microstructure and Compressive Deformation Behavior of Ss Foam Made through Evaporation of Urea as Space Holder. *Mater. Chem. Phys.* **2019**, *223*, 737–744. [[CrossRef](#)]
32. Suzuki, A.; Kosugi, N.; Takata, N.; Kobashi, M. Microstructure and Compressive Properties of Porous Hybrid Materials Consisting of Ductile Al/Ti and Brittle Al₃Ti Phases Fabricated by Reaction Sintering with Space Holder. *Mater. Sci. Eng. A* **2020**, *776*, 139000. [[CrossRef](#)]
33. Zhiwei, D.; Jian, C.; Binna, S. Preparation of SiC/Al Composite Foams by Spark Plasma Sintering and Dissolution and Its Compression Properties. *J. Mater. Metall.* **2019**, *18*, 121–126.
34. Alizadeh, M.; Mirzaei-Aliabadi, M. Compressive Properties and Energy Absorption Behavior of Al–Al₂O₃ Composite Foam Synthesized by Space-Holder Technique. *Mater. Des.* **2012**, *35*, 419–424. [[CrossRef](#)]
35. Yang, X.; Hu, Q.; Du, J.; Song, H.; Zou, T.; Sha, J.; He, C.; Zhao, N. Compression Fatigue Properties of Open-Cell Aluminum Foams Fabricated by Space-Holder Method. *Int. J. Fatigue* **2019**, *121*, 272–280. [[CrossRef](#)]
36. Mondal, D.; Majumder, J.D.; Jha, N.; Badkul, A.; Das, S.; Patel, A.; Gupta, G. Titanium-Cenosphere Syntactic Foam Made through Powder Metallurgy Route. *Mater. Des.* **2012**, *34*, 82–89. [[CrossRef](#)]